A search for transit timing variations in the HATS-18 planetary system

John Southworth [1]★ A. J. Barker [2], T. C. Hinse [3,4] Y. Jongen,[5] M. Dominik [6], U. G. Jørgensen,[7]
P. Longa-Peña,[8] S. Sajadian,[9] C. Snodgrass [10], J. Tregloan-Reed [11], N. Bach-Møller [7,12]
M. Bonavita [10], V. Bozza,[13,14] M. J. Burgdorf,[15] R. Figuera Jaimes,[16] Ch. Helling,[12,17] J. A. Hitchcock [6],
M. Hundertmark,[18] E. Khalouei,[19] H. Korhonen,[20] L. Mancini [21,22,23,24] N. Peixinho,[25] S. Rahvar [26]
M. Rabus [27] J. Skottfelt[28] and P. Spyratos[1]

Affiliations are listed at the end of the paper

ABSTRACT

HATS-18 b is a transiting planet with a large mass and a short orbital period, and is one of the best candidates for the detection of orbital decay induced by tidal effects. We present extensive photometry of HATS-18 from which we measure 27 times of mid-transit. Two further transit times were measured from data from the *Transiting Exoplanet Survey Satellite* (*TESS*) and three more taken from the literature. The transit timings were fitted with linear and quadratic ephemerides and an upper limit on orbital decay was determined. This corresponds to a lower limit on the modified stellar tidal quality factor of $Q'_\star > 10^{5.11\pm0.04}$. This is at the cusp of constraining the presence of enhanced tidal dissipation due to internal gravity waves. We also refine the measured physical properties of the HATS-18 system, place upper limits on the masses of third bodies, and compare the relative performance of *TESS* and the 1.54 m Danish Telescope in measuring transit times for this system.

Key words: stars: fundamental parameters – stars: individual: HATS-18 – planetary systems.

1 INTRODUCTION

The hot Jupiters are a class of extrasolar planet characterized by a relatively large mass and a short orbital period. As a result, they are expected to undergo strong tidal interactions with their host stars (e.g. Ogilvie 2014; Mathis 2019). This will lead to exchanges of angular momentum and energy between the stellar rotation and the planetary orbit. Since the host stars of most hot Jupiters have a rotational frequency below that of their planet's orbital frequency, one manifestation of this interaction is orbital decay: a decrease in the orbital period of the planet and therefore the progressively earlier occurrence of transits in a system. Hence, observations of transit times can constrain the efficiency of such tidal interactions (e.g. Birkby et al. 2014; Maciejewski et al. 2018; Patra et al. 2020). This in turn is relevant as a window on stellar structure (Love 1911) and on the ultimate fate of short-period planets (Jackson, Barnes & Greenberg 2009; Levrard, Winisdoerffer & Chabrier 2009; Matsumura, Peale & Rasio 2010).

It is therefore helpful to search for transit time variations (TTVs) in systems containing hot Jupiters. Because the effects of tides are small on a human time-scale, it is wise to concentrate this search on the most promising systems. Maciejewski et al. (2018) used a result from Goldreich & Soter (1966) to develop an equation giving the expected shift in transit times as a function of the orbital period and mass ratio of a system plus the tidal efficiency and size of the host star (their equation 2). We used this approach to rank all transiting extrasolar

planets (TEPs) in TEPCat[1] in decreasing order of predicted transit shift over a 10-yr period. The planetary system HATS-18 was found to be one of the best candidates, so we embarked on a campaign to determine precise transit times for this system over a period of several years.

HATS-18 was observed in the course of the HATSouth transit survey (Bakos et al. 2013) and its detection and characterization was announced by Penev et al. (2016). It consists of a solar-type star ($1.0\,M_\odot$, $1.0\,R_\odot$) with a gas giant ($2.0\,M_{\rm Jup}$, $1.3\,R_{\rm Jup}$) in an orbit with a very short period (0.838 d). The properties of the system were measured (Penev et al. 2016) based primarily on a single high-quality transit light curve, six high-precision radial velocity (RV) measurements, and predictions from the Yonsei–Yale theoretical stellar evolutionary models (Demarque et al. 2004). Penev et al. (2016) also presented a detailed analysis of the tidal characteristics of the system, highlighting its importance in constraining tidal theory.

There has been little subsequent (published) work on the nature of HATS-18. Patra et al. (2020) presented two times of minimum light obtained using a 60 cm telescope which were consistent with a constant orbital period. The system has also been observed in two sectors by the NASA *Transiting Exoplanet Survey Satellite* (*TESS*; Ricker et al. 2015). We used both data sets in our own analysis in order to obtain the best constraints on the orbital evolution of HATS-18.

Since our work on HATS-18 began, several theoretical studies of tidal dissipation have highlighted the importance of internal gravity waves in hot Jupiter systems and selected HATS-18 as a promising

---

[1]The Transiting Extrasolar Planet Catalogue (Southworth 2011) is at: https://www.astro.keele.ac.uk/jkt/tepcat/

Table 1. Log of the Danish Telescope observations obtained for HATS-18. N_{obs} is the number of observations, T_{exp} is the exposure time, T_{dead} is the dead time between exposures, 'Moon illum.' is the fractional illumination of the Moon at the midpoint of the transit, and N_{poly} is the order of the polynomial fitted to the out-of-transit data. The aperture radii are target aperture, inner sky, and outer sky, respectively.

Date of first observation	Start time (UT)	End time (UT)	N_{obs}	T_{exp} (s)	T_{dead} (s)	Filter	Airmass	Moon illumination	Aperture radii (pixels)	N_{poly}	Scatter (mmag)
2017/05/13	23:07	01:03	48	100–150	13	R	$1.08 \rightarrow 1.00$	0.913	16 24 45	1	1.05
2017/05/29	00:34	04:14	117	100	13	R	$1.01 \rightarrow 1.83$	0.156	13 21 45	1	1.03
2017/06/09	23:29	02:36	100	100	13	R	$1.00 \rightarrow 1.42$	0.996	11 18 40	1	1.56
2017/06/13	23:26	01:58	81	80–100	13	R	$1.01 \rightarrow 1.33$	0.825	12 20 50	1	1.78
2017/06/18	23:31	03:12	110	100	13	R	$1.03 \rightarrow 2.07$	0.331	13 20 40	1	1.15
2017/07/09	22:49	02:00	91	100	25	R	$1.09 \rightarrow 2.22$	0.993	11 18 40	2	1.19
2018/04/24	23:34	03:31	123	100	14	R	$1.20 \rightarrow 1.00 \rightarrow 1.06$	0.735	10 20 40	2	1.06
2018/04/29	23:34	04:13	140	100	14	R	$1.14 \rightarrow 1.00 \rightarrow 1.18$	0.998	9 15 30	2	1.33
2018/05/05	00:50	04:32	117	100	14	R	$1.01 \rightarrow 1.00 \rightarrow 1.31$	0.768	10 20 40	1	1.15
2018/05/20	23:08	02:58	118	100	16	R	$1.04 \rightarrow 1.00 \rightarrow 1.20$	0.374	10 18 40	1	1.28
2018/05/25	23:19	03:30	125	100	16	R	$1.01 \rightarrow 1.00 \rightarrow 1.41$	0.874	10 18 50	1	2.45
2018/06/20	22:50	02:30	109	100	14	R	$1.01 \rightarrow 1.69$	0.564	14 22 50	1	1.36
2019/05/17	01:39	05:14	108	100	16	R	$1.03 \rightarrow 1.94$	0.961	9 18 40	1	1.37
2019/05/22	22:56	01:40	82	85–100	15	R	$1.03 \rightarrow 1.00 \rightarrow 1.02$	0.826	9 16 35	1	1.20
2019/06/01	23:09	02:43	133	60–100	16	R	$1.01 \rightarrow 1.00 \rightarrow 1.31$	0.023	9 16 40	2	1.22
2021/05/14	23:19	03:46	103	100	28	R	$1.02 \rightarrow 1.00 \rightarrow 1.04$	0.094	8 15 30	2	1.13
2021/05/25	01:43	02:55	111	100	15	R	$1.02 \rightarrow 2.25$	0.972	9 16 35	2	1.52
2021/06/04	22:48	02:15	106	100	18	R	$1.01 \rightarrow 1.00 \rightarrow 1.26$	0.246	13 20 40	2	1.80
2021/06/09	23:37	02:53	99	100	18	R	$1.01 \rightarrow 1.00 \rightarrow 1.54$	0.002	10 16 35	2	1.43
2021/06/14	23:32	03:30	80	100	18	R	$1.02 \rightarrow 1.00 \rightarrow 2.09$	0.192	14 20 40	1	2.34

candidate (Barker 2020; Ma & Fuller 2021). Internal gravity waves are likely to be the dominant tidal mechanism in slowly rotating solar-type main-sequence stars with radiative cores (e.g. Barker & Ogilvie 2010; Chernov, Ivanov & Papaloizou 2017; Barker 2020; Ma & Fuller 2021). In particular, the star HATS-18 A is one in which tidally excited gravity waves are marginally predicted to break in the stellar core, depending strongly on the age of the star. When wave breaking occurs, stellar tidal dissipation is predicted to be efficient and can cause planetary orbital decay on Myr time-scales for planets with orbital periods of approximately one day (e.g. Barker & Ogilvie 2010). Such orbital decay is potentially observable in HATS-18, thus supporting our aim to search for TTVs in this system.

It is important to remember that there are multiple possible causes of TTVs. Orbital decay has been confidently detected in only one system, WASP-12 (Hebb et al. 2009; Maciejewski et al. 2016; Patra et al. 2017; Maciejewski et al. 2018). WASP-4 is also known to have a decreasing orbital period (Bouma et al. 2019; Southworth et al. 2019) but the origin of this is not yet settled (Baluev et al. 2020; Bouma et al. 2020; Turner et al. 2022). TTVs can arise due to the light-time effect caused by long-period companions in a system, as has been found for TrES-5 (Maciejewski et al. 2021), WASP-148 (Maciejewski et al. 2020), and HAT-P-26 (von Essen et al. 2019). TTVs can also be caused by apsidal precession (Patra et al. 2017), starspots (Watson & Dhillon 2004; Oshagh et al. 2013), the Applegate mechanism (Applegate 1992; Watson & Marsh 2010), and gravitational perturbations in multiplanetary systems (e.g. Agol et al. 2005; Holman & Murray 2005; Rowe et al. 2014). Some of these effects can also cause changes in the orbital inclination and/or transit duration.

2 OBSERVATIONS

2.1 Danish Telescope

HATS-18 was observed in the 2017, 2018, 2019, and 2021 observing seasons using the Danish 1.54 m telescope and DFOSC imager at ESO La Silla. No observations were performed in 2020 due to the Covid-19 pandemic. In all cases a Cousins R filter was used to maximize the photon rate for this relatively faint star ($V = 14.1$), and the telescope was operated out of focus to improve the photometric precision (Southworth et al. 2009a,b). DFOSC has a field of view of 13.7 arcmin $\times$ 13.7 arcmin at a plate scale of 0.39 arcsec per pixel, but the CCD was typically windowed down to 12 arcmin $\times$ 8 arcmin to decrease the readout time. The autoguider was not used because of technical issues.
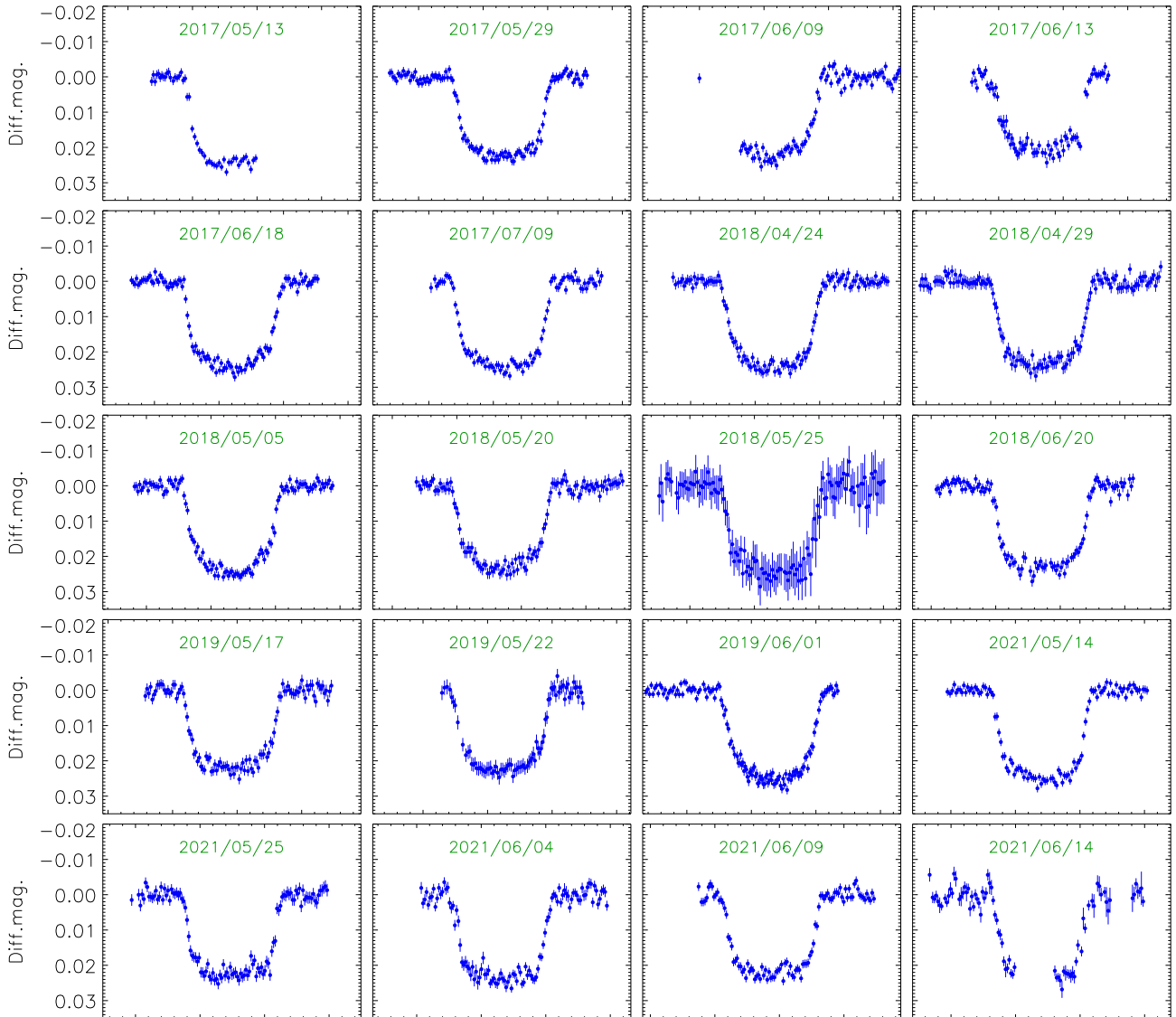
A total of 20 transits were observed and an observing log is given in Table 1. Of the 20 transits, 13 were good, five were affected by atmospheric cloud or haze (2017 May 13, 2017 June 13, 2018 May 25, 2018 June 20, 2021 June 14) and two suffered from technical problems (2017 June 9, 2019 May 22).

Data reduction was performed using the DEFOT pipeline (Southworth et al. 2009a, 2014), which in turn uses routines from the NASA ASTROLIB library[2] IDL[3] implementation of the APER routine from DAOPHOT (Stetson 1987). Image motion was measured by cross-correlating each image with a reference image obtained near the midpoint of that observing sequence. The software apertures were placed by hand on the reference images and the radii of the aperture and sky annulus were chosen manually. No bias or flat-field calibrations were applied, as we found that these had little effect beyond increasing the scatter of the results. Cloud-affected data were rejected when they gave measurements that were unreliable.

Differential-magnitude light curves were constructed by optimizing the weights of between two and five comparison stars simultaneously with a low-order polynomial fitted to the out-of-transit data (Table 1). We consistently found that the choices taken during data reduction (bias, flat-field, aperture size, comparison stars, reference image) had little effect on the shape of the transit in the light curve but could have a significant effect on the scatter. The data are plotted in Fig. 1. We have placed them on the

[2] http://idlastro.gsfc.nasa.gov/
[3] http://www.harrisgeospatial.com/SoftwareTechnology/IDL.aspx

Figure 1. Light curves of HATS-18 obtained using the Danish telescope. In each case the *x*-axis shows 0.2 d centred on the time of minimum measured for that transit, but the BJDs are not shown for clarity. The date of each observation is labelled on the plot.

BJD(TDB) time-scale using routines from Eastman, Siverd & Gaudi (2010).

2.2 Jongen Telescope

Nine transits of HATS-18 were observed in the 2020 season using the Yves Jongen Telescope at Deep Sky Chile. This is a PlaneWave Corrected Dall-Kirkham telescope with an aperture of 430 mm, mounted on a L500 Plane Wave Mount, and equipped with a Moravian 4G CCD camera and EFW 4L-7 filter wheel. This setup has a field of view of 21.0 arcmin ×15.8 arcmin at a plate scale of 0.63 arcsec per pixel. A Chroma imaging IR-UV filter was used, which has a high transmission between 370 and 700 nm.

The data reduction was performed using the MUNIPACK[4] software. This comprised standard calibrations and brightness measurement using aperture photometry. Differential-magnitude light curves were calculated versus five nearby comparison stars.
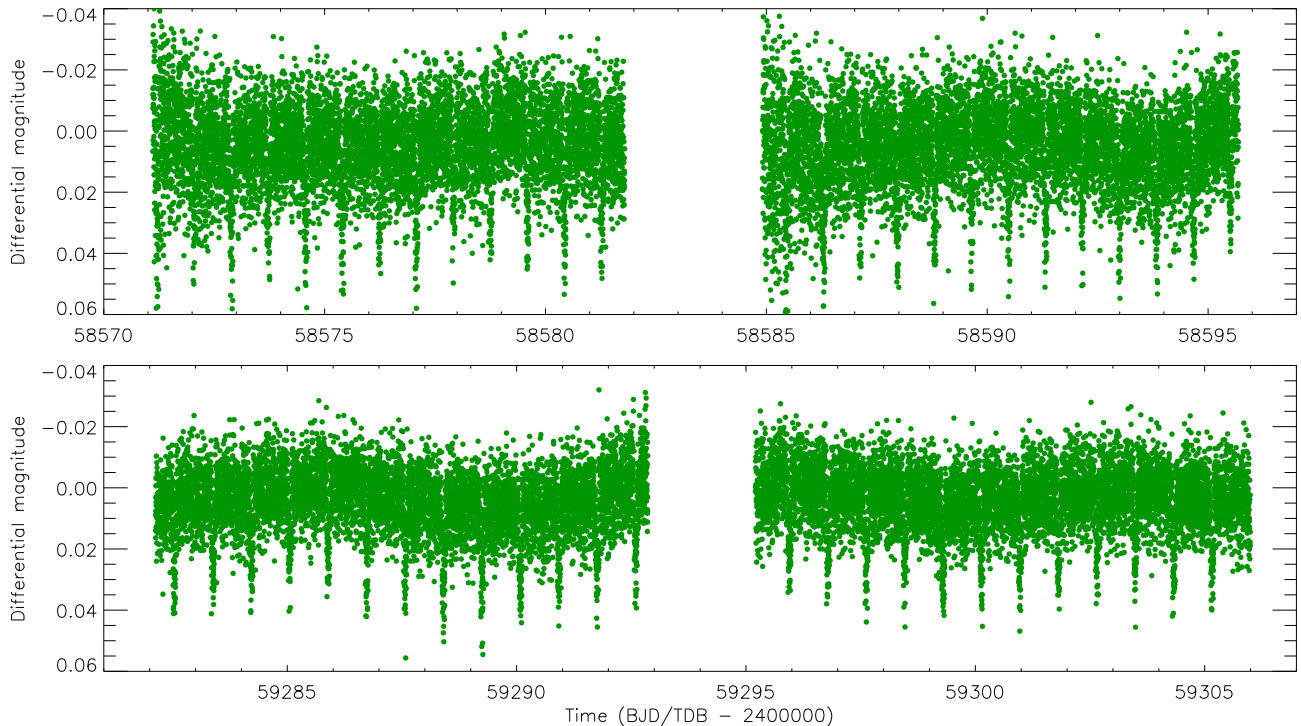
2.3 Transiting Exoplanet Survey Satellite

TESS (Ricker et al. 2015) observed HATS-18 in sectors 10 (2019 March 26 to 2019 April 22) and 36 (2021 March 7 to 2021 April 2). In both sectors it was selected as a short-cadence target. One further observation of HATS-18 with *TESS* is currently scheduled, in sector 69 (2023 March). We downloaded the available observations from the Mikulski Archive for Space Telescopes (MAST) archive[5] and converted them into magnitude units.

We decided to use the pre-search data conditioning (PDCSAP) light curves (Jenkins et al. 2016) rather than the simple aperture photometry (SAP) observations, as they have a slightly lower scatter. We retained only those data points with a QUALITY flag of zero:

[4] https://munipack.physics.muni.cz/

[5] https://mast.stsci.edu/portal/Mashup/Clients/Mast/Portal.html

Figure 2. PDCSAP light curves of HATS-18 from *TESS* sectors 10 (top) and 36 (bottom).

15 390 in sector 10 and 15 449 in sector 36. We further rejected all data points more than 0.24 d (three times the transit duration) from the midpoint of a transit (approximately 71 per cent of the data) as these were not useful for our analysis. The data are quite scattered due to the relative faintness of HATS-18, and the small aperture and large pixel scale of *TESS* (Fig. 2).

3 PHYSICAL PROPERTIES OF HATS-18

The only existing measurement of the physical properties of the HATS-18 system is by Penev et al. (2016), who had access to only one high-quality transit light curve of the system. We have therefore redetermined the physical properties of HATS-18 using our extensive photometry and the methods from the *Homogeneous Studies* project (Southworth 2012, and references therein). The measured parameters are useful in subsequent analyses.

All modelling of the light curves of HATS-18 was done using version 42 of the JKTEBOP[6] code (Southworth 2013, and references therein). We first fitted each transit from the Danish Telescope individually, to check the level of scatter in the light curves. The fitted parameters were the transit midpoint (T_0), the fractional radii of the two components ($r_A = \frac{R_A}{a}$ and $r_b = \frac{R_b}{a}$, where R_A is the radius of the star, R_b is the radius of the planet, and a is the semimajor axis of the relative orbit) expressed as their sum and ratio, and the orbital inclination (i).

Once this was done, we merged the data from the 17 complete transits into a single light-curve file, at the same time scaling the point errors in each data set to obtain $\chi^2_\nu = 1$ versus the best fit. We did not use the three partially observed transits as they are less reliable than the others. We also did not use the transits observed

[6]JKTEBOP is written in FORTRAN77 and the source code is available at http://www.astro.keele.ac.uk/jkt/codes/jktebop.html

with the Jongen Telescope or *TESS* due to their higher scatter. We obtained a best model to the data by fitting for T_0, P, $r_A + r_b$, k, i, and a polynomial function for each transit (see Table 1). This was done for four different two-parameter limb darkening (LD) laws (see Southworth 2008) and with either both coefficients fixed or the linear coefficient fitted. Fixed and initial values of the LD coefficients were taken from the theoretical tabulations by Claret (2000, 2004b, 2017).

The uncertainties in the fitted parameters were calculated using Monte Carlo and residual-permutation simulations (see Southworth 2008). The adopted value of each fitted parameter is the weighted mean of the four fits with one LD coefficient fitted. Its uncertainty is the larger of the Monte Carlo and residual-permutation options, with an additional contribution from the variation in parameter values added in quadrature. These results are given in the top portion of Table 2.

To determine the physical properties of the system an additional constraint is needed (Southworth 2009) for which we resorted to interpolating within tabulated predictions of stellar properties from theoretical models. Measurements of the spectroscopic properties of the host star (temperature $T_{\rm eff}$, metallicity [Fe/H], velocity amplitude K_A) were taken from Penev et al. (2016). We estimated an initial value of the velocity amplitude of the planet K_b and used the measured values of K_A, i, P, r_A, and r_b to determine the physical properties of the system. This process was iterated to find the value of K_b that gave the best match between the observed and predicted $T_{\rm eff}$ and r_A. We included [Fe/H] as a constraint and performed a grid search over age to determine the overall best set of system properties. This process was undertaken for five different sets of theoretical stellar evolutionary models (Claret 2004a; Demarque et al. 2004; Pietrinferni et al. 2004; VandenBerg, Bergbusch & Dowler 2006; Dotter et al. 2008).

Random errors were propagated using a perturbation approach and systematic errors were estimated from the differences between the

Table 2. Derived physical properties of the HATS-18 system. When measurements are accompanied by two errorbars, the first refers to the statistical uncertainty and the second to the systematic uncertainty. The properties from Penev et al. (2016) are included for comparison.

Parameter	Symbol	Unit	This work	Penev et al. (2016)
Orbital period	P	d	$0.83784369 \pm 0.00000011$	$0.83784340 \pm 0.00000047$
Sum of the fractional radii	$r_A + r_b$	–	0.2979 ± 0.0043	–
Ratio of the radii	k	–	0.13426 ± 0.00095	0.1347 ± 0.0019
Orbital inclination	i	°	88.2 ± 1.8	$85.5^{+1.9}_{-2.8}$
Fractional radius of star	r_A	–	0.2627 ± 0.0036	$0.2695^{+0.0090}_{-0.0078}$
Fractional radius of planet	r_b	–	0.03524 ± 0.00065	–
Stellar effective temperature	T_{eff}	K	–	5600 ± 120
Stellar metallicity	[Fe/H]	dex	–	$+0.280 \pm 0.080$
Stellar velocity amplitude	K_A	$m\,s^{-1}$	–	415.2 ± 10.0
Stellar mass	M_A	$M_\odot$	$1.048 \pm 0.057 \pm 0.027$	1.037 ± 0.047
Stellar radius	R_A	$R_\odot$	$0.999 \pm 0.021 \pm 0.009$	$1.020^{+0.057}_{-0.031}$
Stellar surface gravity	$\log g_A$	(cgs)	$4.460 \pm 0.015 \pm 0.004$	4.436 ± 0.034
Stellar density	ρ_A	$\rho_\odot$	1.052 ± 0.043	$0.978^{+0.092}_{-0.149}$
Planetary mass	M_b	M_{Jup}	$1.990 \pm 0.087 \pm 0.034$	1.980 ± 0.077
Planetary radius	R_b	R_{Jup}	$1.304 \pm 0.034 \pm 0.011$	$1.337^{+0.102}_{-0.049}$
Planetary surface gravity	g_b	$m\,s^{-2}$	29.0 ± 1.3	$27.2^{+2.3}_{-3.7}$
Planetary density	ρ_b	ρ_{Jup}	$0.840 \pm 0.053 \pm 0.007$	$0.769^{+0.098}_{-0.151}$
Equilibrium temperature	T'_{eq}	K	2029 ± 45	2060 ± 59
Safronov number	Θ	–	$0.0514 \pm 0.0018 \pm 0.0004$	$0.0498^{+0.0025}_{-0.0033}$
Semimajor axis	a	au	$0.01768 \pm 0.00032 \pm 0.00015$	0.01761 ± 0.00027
Age	τ	Gyr	$3.2^{+2.2+1.7}_{-2.1-1.3}$	4.2 ± 2.2

five sets of solutions using the various theoretical predictions. Our final set of properties of the system are collected in Table 2, which also shows the values from Penev et al. (2016) for comparison. Our new observations have enabled, amongst other results, significantly better measurements of r_A (a parameter important for tidal evolution) and ρ_b (relevant in understanding the structure and evolution of planets). The age determination remains frustratingly uncertain; an improved value might be obtained from a more precise T_{eff} measurement. Although HATS-18 A has a measured rotation period of 9.8 ± 0.4 d (Penev et al. 2016) indicative of a relatively young age, there is evidence that gyrochronological ages are unreliable for the host stars of hot Jupiters (Brown 2014; Poppenhaeger & Wolk 2014; Maxted, Serenelli & Southworth 2015; Mancini et al. 2017).

4 TRANSIT TIMING ANALYSIS

4.1 Measurement of the transit times

We modelled the observed transit light curves individually as detailed in Section 3, fitting for T_0, $r_A + r_b$, $k = \frac{r_b}{r_A}$, i, and the linear LD coefficient of the quadratic LD law. We also included a quadratic polynomial to model the out-of-eclipse brightness of the system, in order to capture the uncertainties in the light-curve normalization process at the data-reduction stage. The two transits from the Danish Telescope lacking coverage of either the ingress or egress (2017 May 13 and 2017 June 9) were not included because such data do not give reliable transit times (e.g. Gibson et al. 2009). Uncertainties on the transit times were obtained using Monte Carlo and residual-permutation simulations (Southworth 2008) and the larger of the two options was used. In cases where the reduced χ^2 of the fit was $\chi^2_\nu > 1$ the errorbar was further multiplied by $\sqrt{\chi^2_\nu}$ to avoid underestimation of the uncertainties.

The *TESS* data demanded a different approach as the scatter is high. We therefore fitted all transits from each sector simultaneously

to determine a single effective time of transit for that sector. The reference time of transit was chosen to be the observed transit closest to the midpoint of the data in each case, and a quadratic polynomial was included to account for slow drifts in the instrumental magnitudes of the system over the sector. The uncertainties were obtained using Monte Carlo simulations.

4.2 Published transit times

Penev et al. (2016, their table 4) presented a single transit time, T_C, from a joint analysis of all the light and radial velocity curves available to them. We did not wish to use this directly as it is measured from data taken over 4 yr so is not suitable for any analysis where the orbital period may be changing. We therefore modelled the one follow-up light curve which has full coverage of a transit, using the same approach as above. This was taken on the night of 2016 January 22 using an LCOGT[7] 1-m telescope and Sinistro imager at the Cerro Tololo Inter-American Observatory (CTIO[8]). The data were reported as BJD on the UTC time system so we converted the resulting transit time to TDB.

We subsequently found that this transit time occurred significantly later than expected (approximately 100 s) from a preliminary orbital ephemeris based on our Danish Telescope data. Dr. Joel Hartman kindly made available the original data for us to reduce using our own DEFOT code. We found that our own light curve has timestamps in excellent agreement with those from Penev et al. (2016), even though ours are expressed in TDB and the published data are given in UTC. Furthermore, our own transit time is in much better agreement with the preliminary orbital ephemeris. We conclude that the timestamps from the published data are actually

[7] https://lco.global/
[8] https://noirlab.edu/public/programs/ctio/

Table 3. All times of mid-transit for HATS-18 used in this work.

BJD(TDB)	Cycle	Residual (s)	Source
2457410.80009 ± 0.00030	− 1451.0	0.00024	This work (Penev et al. 2016 transit)
2457834.74845 ± 0.00040	− 945.0	− 0.00037	Patra et al. (2020)
2457902.61444 ± 0.00019	− 864.0	0.00027	This work (Danish Telescope)
2457918.53333 ± 0.00063	− 845.0	0.00013	This work (Danish Telescope)
2457923.55998 ± 0.00017	− 839.0	− 0.00028	This work (Danish Telescope)
2457944.50658 ± 0.00018	− 814.0	0.00022	This work (Danish Telescope)
2458217.64370 ± 0.00029	− 488.0	0.00026	Patra et al. (2020)
2458233.56286 ± 0.00021	− 469.0	0.00038	This work (Danish Telescope)
2458238.58946 ± 0.00027	− 463.0	− 0.00008	This work (Danish Telescope)
2458243.61625 ± 0.00018	− 457.0	− 0.00035	This work (Danish Telescope)
2458259.53486 ± 0.00027	− 438.0	− 0.00077	This work (Danish Telescope)
2458264.56344 ± 0.00068	− 432.0	0.00074	This work (Danish Telescope)
2458290.53560 ± 0.00024	− 401.0	− 0.00025	This work (Danish Telescope)
2458581.26804 ± 0.00043	− 54.0	0.00038	This work (*TESS*)
2458620.64595 ± 0.00021	− 7.0	− 0.00037	This work (Danish Telescope)
2458626.51102 ± 0.00045	0.0	− 0.00021	This work (Danish Telescope)
2458636.56579 ± 0.00020	12.0	0.00044	This work (Danish Telescope)
2458898.81064 ± 0.00036	325.0	0.00017	This work (Jongen Telescope)
2458862.78435 ± 0.00068	282.0	0.00117	This work (Jongen Telescope)
2458883.72975 ± 0.00048	307.0	0.00047	This work (Jongen Telescope)
2458903.83713 ± 0.00054	331.0	− 0.00040	This work (Jongen Telescope)
2458950.75579 ± 0.00088	387.0	− 0.00099	This work (Jongen Telescope)
2458972.54162 ± 0.00046	413.0	0.00090	This work (Jongen Telescope)
2458982.59355 ± 0.00078	425.0	− 0.00130	This work (Jongen Telescope)
2459034.54221 ± 0.00069	487.0	0.00105	This work (Jongen Telescope)
2459292.59679 ± 0.00029	795.0	− 0.00027	This work (*TESS*)
2459203.78668 ± 0.00079	689.0	0.00107	This work (Jongen Telescope)
2459349.57034 ± 0.00020	863.0	− 0.00010	This work (Danish Telescope)
2459359.62471 ± 0.00021	875.0	0.00015	This work (Danish Telescope)
2459370.51596 ± 0.00040	888.0	− 0.00057	This work (Danish Telescope)
2459375.54404 ± 0.00042	894.0	0.00044	This work (Danish Telescope)
2459380.57024 ± 0.00058	900.0	− 0.00042	This work (Danish Telescope)

in TDB, not UTC. For subsequent analysis we therefore used our measurement of the transit time, from the light curve presented by Penev et al. (2016), under the assumption that the timestamps are in TDB.

Two further transit times of HATS-18 were given by Patra et al. (2020). These are already in BJD/TDB so were added to our analysis without modification. We are not aware of any further source of transit times for this system.

4.3 Orbital ephemerides

Once the transit times were assembled we fitted them with a straight line to obtain a linear ephemeris:

$$T_0 = \text{BJD(TDB)} \ 2458626.511225(71) + 0.83784382(11) \times E,$$

where E is the epoch of the transit and the bracketed quantities indicate the uncertainties in the preceding digits. The fit has $\chi_\nu^2 = 1.79$, which is significantly larger than the 1.0 expected for a good fit but in line with our past experience that χ_ν^2 is usually more than 1.0 in this kind of analysis (e.g. Southworth et al. 2016; Baştürk et al. 2022). The 1σ uncertainties in the ephemeris above have been multiplied by $\sqrt{\chi_\nu^2}$ to account for this relatively poor fit. The transit times and their residuals are given in Table 3.

Once the linear ephemeris was established, we tried fitting for quadratic and cubic ephemerides of the forms

$$T_0 = T_{\text{ref}} + P E + p_1 E^2$$

and

$$T_0 = T_{\text{ref}} + P E + p_1 E^2 + p_2 E^3,$$

where p_1 and p_2 are the coefficients of the quadratic and cubic terms, respectively. These give a very similar fit, with slightly larger values for the Bayesian Information Criterion (BIC; Schwarz 1978; Liddle 2007) and Akaike Information Criterion (AIC; Akaike 1974) than the linear ephemeris. The properties of these fits are compared with the linear ephemeris in Table 4 and shown graphically in Fig. 3. The uncertainties in the fitted coefficients were determined using 10 000 Monte Carlo simulations, which were found to be in excellent agreement with the formal errors outputted by the fitting code.[9]

The curvature term in the quadratic ephemeris represents a period decrease which could be attributed to tidally induced orbital decay if it were negative. Instead it can be seen that this term is positive but consistent with zero. The cubic ephemeris is designed to allow the detection of a changing acceleration which could be attributed to orbital motion with a third body in the system. However, the quadratic and cubic ephemerides are not a significantly better fit to the data than the linear ephemeris, so we are only able to set upper limits on orbital period changes. Future monitoring of the system is needed to refine these limits and push the noise down below any real astrophysical signal.

Finally, we used the PERIOD04 package (Lenz & Breger 2005) to check for periodic variations in the residuals of the timings versus

[9]To fit the ephemerides we used the POLY_FIT routine in IDL.

Table 4. Properties of the ephemerides calculated in this work. The linear ephemeris was adopted as the final one.

Quantity	Linear ephemeris (adopted)	Quadratic ephemeris	Cubic ephemeris
Reference time (BJD/TDB)	2458626.51123 (7)	2458626.51120 (10)	2458626.51129 (13)
Linear term (d)	0.83784382 (11)	0.83784382 (11)	0.83784404 (22)
Quadratic term (p_1)	–	$(0.6 \pm 1.7) \times 10^{-10}$	$(-1.2 \pm 2.3) \times 10^{-10}$
Cubic term (p_2)	–	–	$(-2.9 \pm 2.5) \times 10^{-13}$
r.m.s. of residuals (s)	50.2	50.2	49.5
BIC	64.2	67.5	68.7
AIC	61.3	63.1	62.9
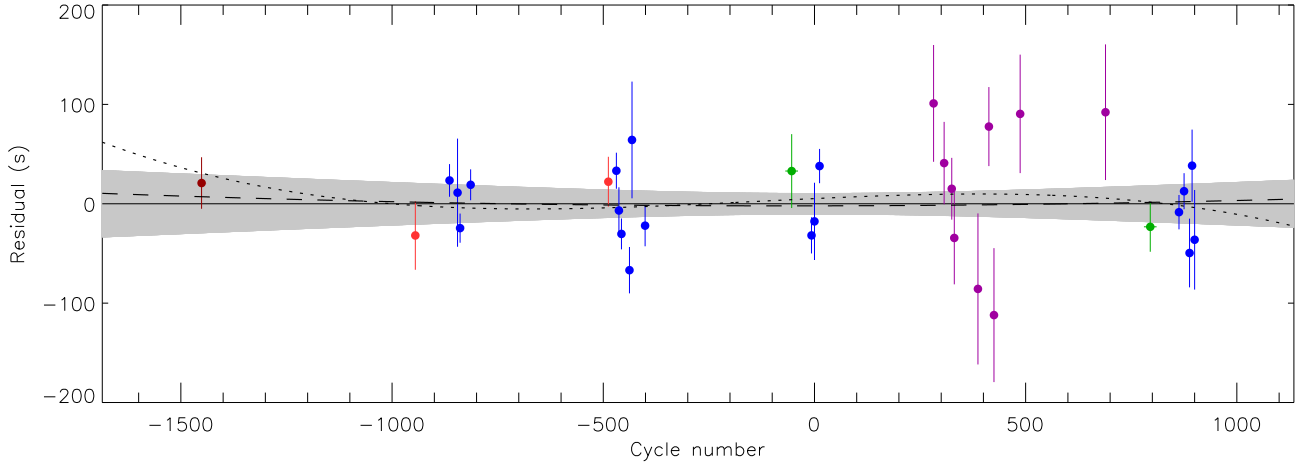
Figure 3. Plot of the residuals of the timings of mid-transit versus a linear ephemeris. Light red points indicate published timings, the dark red point is our analysis of the transit light curve from Penev et al. (2016), blue points are timings from the Danish Telescope, purple from the Jongen Telescope, and green from *TESS*. The dashed line indicates the difference between the best-fitting linear and quadratic ephemerides, and the dotted line the difference between the linear and cubic ephemerides. The grey shade indicates the uncertainty in the linear ephemeris as a function of orbital cycle.

the linear ephemeris. No significant signals were found, with the strongest being at 0.0545 cycle^{-1} with a signal-to-noise ratio of 2.9, well below the commonly used signal-to-noise ratio threshold of 4.0 (Breger et al. 1993). We therefore find no evidence in our data for a periodic variation in the times of transit for HATS-18.

4.4 Constraints on the tidal quality factor

The tidal quality factor, $Q_\star$, is a measure of the efficiency of the dissipation of tidal energy (e.g. Ogilvie 2014). To constrain $Q_\star$, we followed the approach from Birkby et al. (2014), which refers to the modified tidal quality factor

$$Q_\star' = \frac{3}{2} \frac{Q_\star}{k_2},$$

where k_2 is the Love number (Love 1911). This is related to measurable properties of the system via the equation

$$Q_\star' = \frac{-27}{8} \left(\frac{M_b}{M_A}\right) \left(\frac{R_A}{a}\right)^5 \left(\frac{2\pi}{P_{orb}}\right) \frac{1}{p_1}$$

(Wilkins et al. 2017), where (R_A/a) is simply r_A, p_1 is the quadratic coefficient in the ephemeris, and the other terms have the meanings given in Table 2.

Our value of p_1 in Table 4 is greater than zero (i.e. it indicates an increasing orbital period) so would cause a negative $Q_\star'$ if inserted blindly into the equation above. We therefore used its 3σ lower limit of $p_1^{lim} = -4.5 \times 10^{-10}$ to obtain the constraint that $Q_\star' > 10^{5.11 \pm 0.04}$, where the errorbar comes from propagating the uncertainties in M_A, M_b, and r_A. This limit is comparable to previous

constraints for other systems (e.g. Ogilvie & Lin 2007; Jackson, Greenberg & Barnes 2008; Penev et al. 2012).

4.5 Comparison of the tidal quality factor with models for stellar tidal dissipation

HATS-18 is a 1.05 $M_\odot$ G-star and so it likely harbours a radiative core on the main sequence. It also rotates much slower than the planetary orbit: based on $v\sin i = 6.23$ km s^{-1} (Penev et al. 2016), we obtain a lower bound on the stellar rotation period of approximately 8 d (cf. 9.8 d in Penev et al. 2016). Hence, the dominant tidal mechanism is expected to be excitation and dissipation of internal gravity waves launched from the radiative/convective interface into the radiative core (e.g. Goodman & Dickson 1998; Ogilvie & Lin 2007; Barker & Ogilvie 2010; Chernov et al. 2017; Barker 2020). Hydrodynamical simulations show that if these waves have large enough amplitudes to break, they are efficiently damped (Barker & Ogilvie 2010; Barker 2011), so we may then estimate tidal dissipation rates by assuming these waves are completely absorbed. This gives a simple estimate for the stellar tidal quality factor $Q_\star'$ (see e.g. equation 41 of Barker 2020), that can be computed using stellar models together with the currently observed planetary mass and orbital period (note: $Q_\star' \propto P_{orb}^{8/3}$).

The critical planetary mass required to cause wave breaking in the stellar core is predicted to be a strong function of stellar age (and mass). To explore this scenario, we computed the evolution of HATS-18 using MESA stellar models (r12278, using an initial mass 1.05 $M_\odot$ and metallicity $Z = 0.03$; Paxton et al. 2011, 2013, 2015, 2018, 2019) and evaluated the critical planetary mass M_{crit} required to initiate
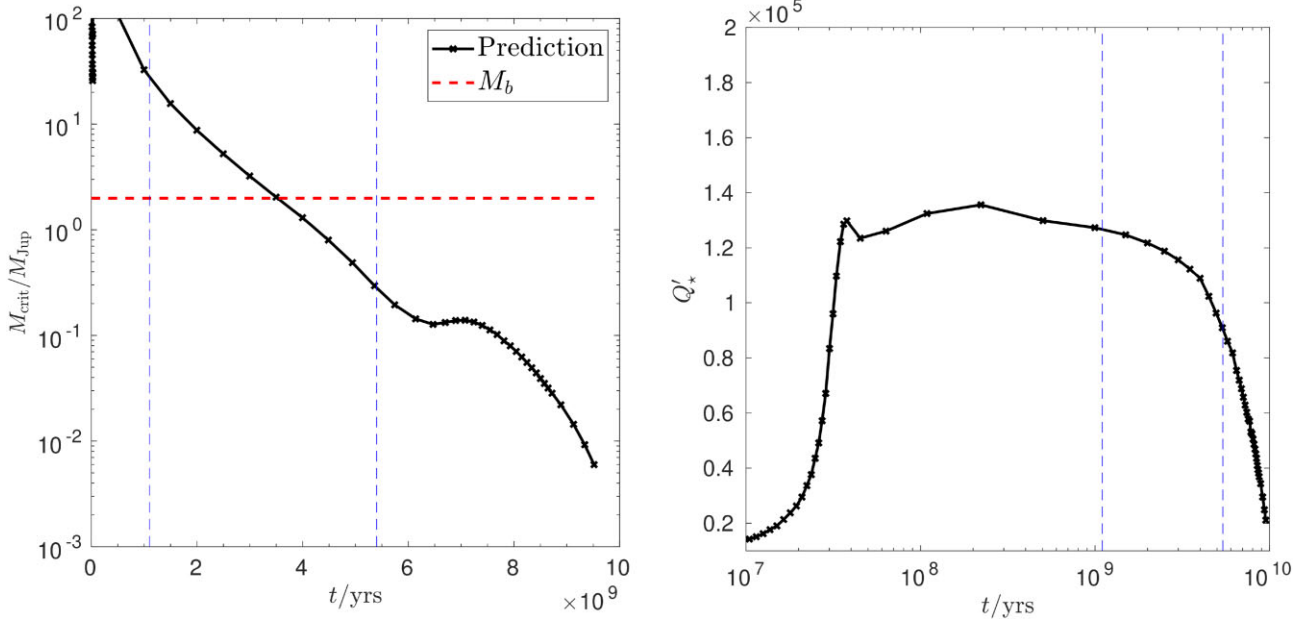
Figure 4. Left-hand panel: critical planetary mass $M_{\rm crit}$ for gravity wave breaking in $M_{\rm Jup}$ as a function of stellar age t (in yr) in a model of HATS-18. The red dashed line indicates the mass of HATS-18 b ($M_b = 2\,M_{\rm Jup}$). Right-hand panel: $Q'_\star$ due to tidally excited gravity waves as a function of stellar age t (in yr), based on the current orbital period. The blue dashed lines indicate the uncertainty in stellar age in Table 2.

wave breaking by applying equation (47) in Barker (2020). Results for $M_{\rm crit}/M_{\rm Jup}$ are shown in Fig. 4 (left-hand panel) as a function of stellar age. This shows that wave breaking is not predicted for ages less than 3.5 Gyr, since $M_{\rm crit}$ exceeds the observed planetary mass (red dashed line). For ages older than 3.5 Gyr, wave breaking is expected in the stellar core, and we show the resulting $Q'_\star$ prediction as a function of age in Fig. 4 (right-hand panel). We typically find $Q'_\star \approx 1.2 \times 10^5 \approx 10^{5.08}$ for ages less than approximately 3 Gyr (similar to the predictions in Barker 2020). Since we have constrained $Q'_\star \gtrsim 10^{5.11}$, our prediction that $Q'_\star \approx 1.5 \times 10^5 \approx 10^{5.08}$ is right at the limit of what can be tested by the available observations.

For earlier ages, or in general for cases where wave breaking is not predicted, gravity waves are likely to be much more weakly damped by radiative diffusion, with correspondingly much larger $Q'_\star$. Alternatively, weaker non-linear effects such as parametric instabilities could be important, though tidal dissipation rates from these are hard to predict with certainty (e.g. Barker & Ogilvie 2011; Weinberg et al. 2012; Essick & Weinberg 2016). On the other hand, if it is possible to enter the fully damped regime for gravity waves through processes other than wave breaking (as predicted above), theory would again predict $Q'_\star \approx 10^{5.08}$. Such processes include gradual spin-up of the core due to radiative diffusion (Barker & Ogilvie 2010), and perhaps by wave breaking (for lower tidal amplitudes) initiated by passage through a resonance (e.g. Ma & Fuller 2021, since wave breaking would likely prohibit resonance locking). This system therefore remains a very interesting one for follow-up studies with further observations having a strong potential to test tidal theory.

4.6 Determining the upper mass limit of a hypothetical perturber

Having transit timing measurements gives an opportunity to place constraints on the upper mass limit of a hypothetical planetary companion. The amplitude of the timing residuals is directly pro-

portional to the mass of the perturber for a given orbital distance. The root-mean-square (RMS) statistic of the timing residuals offers a reasonable estimate of the amplitude which enables an estimate of the upper mass limit of a putative perturbing body. Any TTV effect is amplified for orbital configurations involving mean-motion resonances (Agol et al. 2005; Holman & Murray 2005; Nesvorný & Morbidelli 2008) and should allow the detection of a low-mass planetary perturbing body. A larger perturbation implies a larger RMS scatter around the nominal ephemeris.

The applied method followed the technique described in Wang et al. (2017, 2018a,b). The calculation of an upper mass limit was performed numerically via direct orbit integrations of the equations of motion. For this task, we modified the FORTRAN-based MICROFARM[10] package (Goździewski 2003; Goździewski, Breiter & Borczyk 2008) which relies on OPENMPI[11] to spawn several parallel tasks. The package's main purpose is the numerical computation of the Mean Exponential Growth factor of Nearby Orbits (MEGNO; Cincotta & Simó 2000; Goździewski et al. 2001; Cincotta, Giordano & Simó 2003) over a grid of initial conditions of orbital parameters. In this work, we followed a direct brute-force method for the calculation of the RMS statistic.

We integrated the orbit of HATS-18 within the framework of the general three-body problem. The mid-transit time was calculated iteratively to a high precision from a series of back-and-forth integrations once a transit of HATS-18 b was detected. The best-fitting radii of both the planet and the host star were accounted for. We then calculated an analytic least-squares regression to the time series of transit numbers and mid-transit times to determine a best-fitting linear ephemeris with an associated RMS statistic for the TTVs. The RMS statistic was based on a 25 yr integration corresponding to 8711 transits by HATS-18 b. This procedure was then applied to a grid of masses and semimajor axes of the perturbing planet while

[10]https://bitbucket.org/chdianthus/microfarm/src
[11]https://www.open-mpi.org
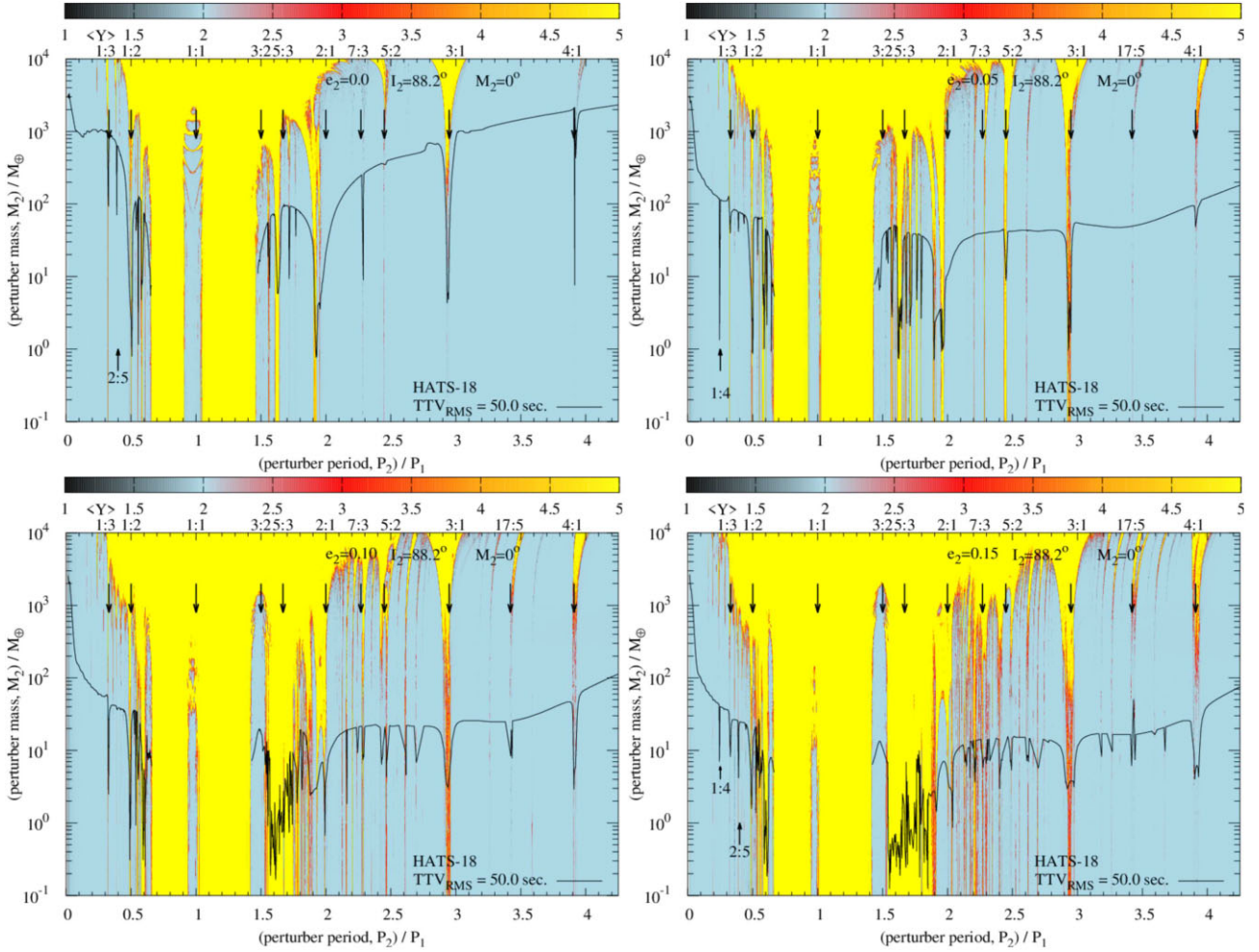
Figure 5. Dynamical (heat) maps based on MEGNO and upper mass limit (solid line) of a putative perturbing body for an observed TTV RMS statistic of 50 s as determined in this study. We considered four different initial eccentricities for the perturbing planet.

fixing all the other orbital parameters. In this study, we chose to start the putative perturbing planet on a circular orbit that is coplanar with HATS-18 b. This implies that $\Omega_2 = 0°$ and $\omega_2 = 0°$ for the perturber and $\Omega_1 = 0°$ for the transiting planet. This setting provides the most conservative estimate of the upper mass limit of a possible perturber (Bean 2009; Fukui et al. 2011; Hoyer et al. 2011; Hoyer, Rojo & López-Morales 2012). We refer the interested reader to Wang et al. (2018a), who studied the effects of TTVs on varying initial orbital parameters of the perturbing body.

In order to calculate the location of mean-motion resonances, we used the same code to calculate MEGNO on the same parameter grid. However, this time we integrated each initial grid point for 1000 yr, which was found to be long enough to allow detection of the location of weak chaotic high-order mean-motion resonances.

Briefly, the MEGNO factor $\langle Y(t) \rangle$ quantitatively measures the degree of stochastic behaviour of a non-linear dynamical system and has proven useful in the detection of chaotic resonances (Goździewski et al. 2001; Hinse et al. 2010). In addition to the Newtonian equations of motion, the associated variational equations are solved simultaneously at each integration time-step. The MICROFARM package implements the ODEX[12] extrapolation algorithm

to numerically solve the system of first-order differential equations. This algorithm is slow but robust even for high-eccentricity orbits as well as close encounters. When presenting results (Fig. 5) we always plot the time-averaged MEGNO that is utilized to quantitatively differentiate between quasi-periodic and chaotic dynamics. We refer to Hinse et al. (2010) for a short review of the essential properties of MEGNO.

In a dynamical system that evolves quasi-periodically in time the quantity $\langle Y \rangle$ will asymptotically approach 2.0 for $t \to \infty$. In that case, the orbital elements associated with that orbit are often bounded. In the case of a chaotic time evolution the quantity $\langle Y \rangle$ diverges away from 2.0, with orbital parameters exhibiting erratic temporal excursions. For quasi-periodic orbits, we typically find $|\langle Y \rangle - 2.0|$ to be less than 0.001 at the end of each integration.

Results are shown in Fig. 5 as MEGNO heat maps considering four different initial values in eccentricity for the putative perturbing planet. In each case, we find the usual instability region located in the proximity of the transiting planet (1:1 resonance) with MEGNO colour-coded as yellow (corresponding to $\langle Y \rangle > 5$). The extent of these regions coincides with the results presented in Barnes & Greenberg (2006). The locations of mean-motion resonances are indicated by arrows in each map.

We find that a perturbing body (initial circular orbit) of upper mass limit of around $1–10\,M_\oplus$ will cause an RMS of the measured

52 s when located in the $P_2/P_1 = 2{:}1, 7{:}3, 5{:}2, 3{:}1$, and 4:1 exterior resonance with HATS-18 b. For the 1:3 and 1:2 interior resonance, perturber upper mass limits of $100 \, M_\oplus$ and $1 \, M_\oplus$, respectively, could also cause an RMS mid-transit time scatter of 52 s. However, although we determined upper mass limits, in Section 4.3 we found no compelling evidence for any periodicities that can be attributed to an additional (non-transiting) planet within the HATS-18 system.

5 SUMMARY AND CONCLUSIONS

HATS-18 consists of a massive planet ($2 \, M_{\mathrm{Jup}}$) on a very short-period orbit (0.838 d) around a cool star (5600 K) with a convective envelope. It is a promising candidate for the detection of orbital decay due to tidal effects (Penev et al. 2016), particularly as it is at the cusp of experiencing enhanced tidal dissipation due to internal gravity waves (Barker 2020; Ma & Fuller 2021). We have obtained light curves of 20 transits from the 1.5 m Danish Telescope and nine transits from the Jongen Telescope. We measured 27 times of mid-transit from these data, plus two timings from the *TESS* light curves of HATS-18 in sectors 10 and 36. Together with three published measurements, this gives a total of 32 transit timings available for the system.

The transit timings were fitted with several ephemerides in three functional forms (linear, quadratic, and cubic), with the finding that the linear ephemeris represents them best. This equates to a non-detection of orbital decay which can be used to put an upper limit on the tidal quality factor of the star, $Q'_\star = 10^{5.11 \pm 0.04}$. This constraint is similar to our theoretical predictions in Section 4.5 if wave breaking occurs (or gravity waves are otherwise fully damped). This system therefore remains a very interesting one for follow-up studies with further observations having a strong potential to test tidal theory. One further sector of *TESS* data will (hopefully) become available in mid-2023, and additional ground-based timing measurements will help us to strengthen the detection limit for orbital decay.

We have also obtained revised measurements of the physical properties of the HATS-18 system which are in agreement with and improve on previous results. This part of the analysis was based on the data from the Danish telescope only, due to the higher precision of the observations. This prompted us to make a comparison between the light curves from the Danish telescope and *TESS*. The Danish telescope has an aperture of diameter 154 cm and was used to observe 20 transits from the ground. *TESS* has a single-camera aperture of diameter 10.5 cm and observed 52 transits over two sectors from space. We normalized each transit to zero differential magnitude, converted them into orbital phase, and binned them into bins of duration 120 s. The results are shown in Fig. 6. It is clear that the ground-based observations are greatly superior to the space-based ones for a star of this relatively faint magnitude ($V = 14.1$ and $i = 13.8$; Henden et al. 2012). This is due to the much larger aperture, which lowers photon noise, and finer pixel scale, which lowers noise from the sky background even when the telescope is operated out of focus.
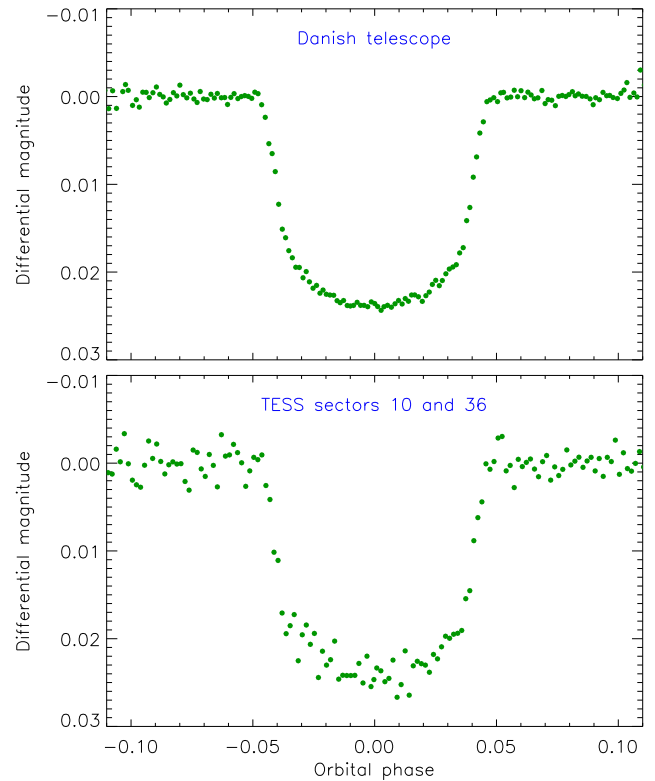
Figure 6. Transit observations of HATS-18 from the Danish Telescope (upper panel) and *TESS* (lower panel). Each data set has been converted into orbital phase then combined into bins of size 120 s.

DATA AVAILABILITY

The light curves obtained with the Danish and Jongen telescopes will be made available at the Centre de Données astronomiques de Strasbourg (CDS) at http://cdsweb.u-strasbg.fr/. The *TESS* data used in this article are available in the MAST archive (https://mast.stsci.edu/portal/Mashup/Clients/Mast/Portal.html).

REFERENCES

Agol E., Steffen J., Sari R., Clarkson W., 2005, MNRAS, 359, 567

Akaike H., 1974, IEEE Trans. Autom. Control, 19, 716

Applegate J. H., 1992, ApJ, 385, 621

Bakos G. Á. et al., 2013, PASP, 125, 154

Baluev R. V. et al., 2020, MNRAS, 496, L11

Barker A. J., 2011, MNRAS, 414, 1365

Barker A. J., 2020, MNRAS, 498, 2270

Barker A. J., Ogilvie G. I., 2010, MNRAS, 404, 1849

Barker A. J., Ogilvie G. I., 2011, MNRAS, 417, 745

Barnes R., Greenberg R., 2006, ApJ, 647, L163

Baştürk Ö. et al., 2022, MNRAS, 512, 2062

Bean J. L., 2009, A&A, 506, 369

Birkby J. L. et al., 2014, MNRAS, 440, 1470

Bouma L. G. et al., 2019, AJ, 157, 217

Bouma L. G., Winn J. N., Howard A. W., Howell S. B., Isaacson H., Knutson H., Matson R. A., 2020, ApJ, 893, L29

Breger M. et al., 1993, A&A, 271, 482

Brown D. J. A., 2014, MNRAS, 442, 1844

Chernov S. V., Ivanov P. B., Papaloizou J. C. B., 2017, MNRAS, 470, 2054

Cincotta P. M., Simó C., 2000, A&AS, 147, 205

Cincotta P. M., Giordano C. M., Simó C., 2003, Phys. D Nonlin. Phenom., 182, 151

Claret A., 2000, A&A, 363, 1081

Claret A., 2004a, A&A, 424, 919

Claret A., 2004b, A&A, 428, 1001

Claret A., 2017, A&A, 600, A30

Demarque P., Woo J.-H., Kim Y.-C., Yi S. K., 2004, ApJS, 155, 667

Dotter A., Chaboyer B., Jevremović D., Kostov V., Baron E., Ferguson J. W., 2008, ApJS, 178, 89

Eastman J., Siverd R., Gaudi B. S., 2010, PASP, 122, 935

Essick R., Weinberg N. N., 2016, ApJ, 816, 18

Fukui A. et al., 2011, PASJ, 63, 287

Gibson N. P. et al., 2009, ApJ, 700, 1078

Goldreich P., Soter S., 1966, Icarus, 5, 375

Goodman J., Dickson E. S., 1998, ApJ, 507, 938

Goździewski K., 2003, A&A, 398, 315

Goździewski K., Bois E., Maciejewski A. J., Kiseleva-Eggleton L., 2001, A&A, 378, 569

Goździewski K., Breiter S., Borczyk W., 2008, MNRAS, 383, 989

Hebb L. et al., 2009, ApJ, 693, 1920

Henden A. A., Levine S. E., Terrell D., Smith T. C., Welch D., 2012, J. Am. Assoc. Var. Star Obs., 40, 430

Hinse T. C., Christou A. A., Alvarellos J. L. A., Goździewski K., 2010, MNRAS, 404, 837

Holman M. J., Murray N. W., 2005, Science, 307, 1288

Hoyer S., Rojo P., López-Morales M., Díaz R. F., Chambers J., Minniti D., 2011, ApJ, 733, 53

Hoyer S., Rojo P., López-Morales M., 2012, ApJ, 748, 22

Jackson B., Greenberg R., Barnes R., 2008, ApJ, 678, 1396

Jackson B., Barnes R., Greenberg R., 2009, ApJ, 698, 1357

Jenkins J. M. et al., 2016, in Chiozzi G., Guzman J. C., eds, Proc. SPIE Conf. Ser. Vol. 9913, Software and Cyberinfrastructure for Astronomy IV. SPIE, Bellingham, p. 99133E

Lenz P., Breger M., 2005, Commun. Asteroseismol., 146, 53

Levrard B., Winisdoerffer C., Chabrier G., 2009, ApJ, 692, L9

Liddle A. R., 2007, MNRAS, 377, L74

Love A. E. H., 1911, Some Problems of Geodynamics. Cambridge Univ. Press, Cambridge, UK

Ma L., Fuller J., 2021, ApJ, 918, 16

Maciejewski G. et al., 2016, A&A, 588, L6

Maciejewski G. et al., 2018, AcA, 68, 371

Maciejewski G., Fernández M., Sota A., García Segura A. J., 2020, AcA, 70, 203

Maciejewski G., Fernández M., Aceituno F., Ramos J. L., Dimitrov D., Donchev Z., Ohlert J., 2021, A&A, 656, A88

Mancini L. et al., 2017, MNRAS, 465, 843

Mathis S., 2019, EAS Publ. Ser., 82, 5

Matsumura S., Peale S. J., Rasio F. A., 2010, ApJ, 725, 1995

Maxted P. F. L., Serenelli A. M., Southworth J., 2015, A&A, 577, A90

Nesvorný D., Morbidelli A., 2008, ApJ, 688, 636

Ogilvie G. I., 2014, ARA&A, 52, 171

Ogilvie G. I., Lin D. N. C., 2007, ApJ, 661, 1180

Oshagh M., Santos N. C., Boisse I., Boué G., Montalto M., Dumusque X., Haghighipour N., 2013, A&A, 556, A19

Patra K. C., Winn J. N., Holman M. J., Yu L., Deming D., Dai F., 2017, AJ, 154, 4

Patra K. C. et al., 2020, AJ, 159, 150

Paxton B., Bildsten L., Dotter A., Herwig F., Lesaffre P., Timmes F., 2011, ApJS, 192, 3

Paxton B. et al., 2013, ApJS, 208, 4

Paxton B. et al., 2015, ApJS, 220, 15

Paxton B. et al., 2018, ApJS, 234, 34

Paxton B. et al., 2019, ApJS, 243, 10

Penev K., Jackson B., Spada F., Thom N., 2012, ApJ, 751, 96

Penev K. et al., 2016, AJ, 152, 127

Pietrinferni A., Cassisi S., Salaris M., Castelli F., 2004, ApJ, 612, 168

Poppenhaeger K., Wolk S. J., 2014, A&A, 565, L1

Ricker G. R. et al., 2015, J. Astron. Telesc. Instrum. Syst., 1, 014003

Rowe J. F. et al., 2014, ApJ, 784, 45

Schwarz G., 1978, Ann. Stat., 5, 461

Southworth J., 2008, MNRAS, 386, 1644

Southworth J., 2009, MNRAS, 394, 272

Southworth J., 2011, MNRAS, 417, 2166

Southworth J., 2012, MNRAS, 426, 1291

Southworth J., 2013, A&A, 557, A119

Southworth J. et al., 2009a, MNRAS, 396, 1023

Southworth J. et al., 2009b, MNRAS, 399, 287

Southworth J. et al., 2014, MNRAS, 444, 776

Southworth J. et al., 2016, MNRAS, 457, 4205

Southworth J. et al., 2019, MNRAS, 490, 4230

Stetson P. B., 1987, PASP, 99, 191

Turner J. D., Flagg L., Ridden-Harper A., Jayawardhana R., 2022, AJ, 163, 281

VandenBerg D. A., Bergbusch P. A., Dowler P. D., 2006, ApJS, 162, 375

von Essen C. et al., 2019, A&A, 628, A116

Wang S. et al., 2018b, AJ, 156, 181

Wang Y.-H. et al., 2017, AJ, 154, 49

Wang X.-Y. et al., 2018a, PASP, 130, 064401

Watson C. A., Dhillon V. S., 2004, MNRAS, 351, 110

Watson C. A., Marsh T. R., 2010, MNRAS, 405, 2037

Weinberg N. N., Arras P., Quataert E., Burkart J., 2012, ApJ, 751, 136

Wilkins A. N., Delrez L., Barker A. J., Deming D., Hamilton D., Gillon M., Jehin E., 2017, ApJ, 836, L24

[1]*Astrophysics Group, Keele University, Staffordshire ST5 5BG, UK*

[2]*Department of Applied Mathematics, School of Mathematics, University of Leeds, Leeds LS2 9JT, UK*

[3]*Institute of Astronomy, Faculty of Physics, Astronomy and Informatics, Nicolaus Copernicus University, ul. Grudziadzka 5, PL-87-100 Toruń, Poland*

[4]*Chungnam National University, Department of Astronomy, Space Science and Geology, Daejeon, South Korea*

[5]*Observatoire de Vaison-La-Romaine, Départementale 51, près du Centre Equestre au Palis, F-84110 Vaison-La-Romaine, France*

[6]*Centre for Exoplanet Science, SUPA, School of Physics and Astronomy, University of St Andrews, North Haugh, St Andrews KY16 9SS, UK*

[7]*Centre for ExoLife Sciences, Niels Bohr Institute, University of Copenhagen, Øster Voldgade 5, DK-1350 Copenhagen, Denmark*

[8]*Centro de Astronomía, CITEVA, Universidad de Antofagasta, Av. Angamos 601, Antofagasta, Chile*

[9]*Department of Physics, Isfahan University of Technology, Isfahan 84156-83111, Iran*

[10]*Institute for Astronomy, University of Edinburgh, Royal Observatory, Edinburgh EH9 3HJ, UK*

[11]*Instituto de Astronomia y Ciencias Planetarias de Atacama, Universidad de Atacama, Copayapu 485, Copiapo, Chile*

[12]*Space Research Institute, Austrian Academy of Sciences, Schmiedlstrasse 6, A-8042 Graz, Austria*

[13]*Dipartimento di Fisica 'E.R. Caianiello', Università di Salerno, Via Giovanni Paolo II 132, I-84084 Fisciano, Italy*

[14]*Istituto Nazionale di Fisica Nucleare, Sezione di Napoli, Napoli, Italy*

[15]*Universität Hamburg, Faculty of Mathematics, Informatics and Natural Sciences, Bundesstraße 55, D-20146 Hamburg, Germany*

[16]*Facultad de Ingeniería y Tecnología, Universidad San Sebastian, General Lagos 1163, Valdivia 5110693, Chile*

[17]*TU Graz, Fakultät für Mathematik, Physik und Geodäsie, Petersgasse 16, A-8010 Graz, Austria*

[18]*Astronomisches Rechen-Institut, Zentrum für Astronomie der Universität Heidelberg (ZAH), D-69120 Heidelberg, Germany*

[19]*Astronomy Research Center, Research Institute of Basic Sciences, Seoul National University, 1 Gwanak-ro, Gwanak-gu, Seoul 08826, Korea*

[20]*European Southern Observatory (ESO), Alonso de Córdova 3107, Vitacura, Santiago, Chile*

[21]*Department of Physics, University of Rome 'Tor Vergata', Via della Ricerca Scientifica 1, I-00133 Rome, Italy*

[22]*Max Planck Institute for Astronomy, K'onigstuhl 17, D-69117 Heidelberg, Germany*

[23]*INAF – Turin Astrophysical Observatory, via Osservatorio 20, I-10025 Pino Torinese, Italy*

[24]*International Institute for Advanced Scientific Studies (IIASS), Via G. Pellegrino 19, I-84019 Vietri sul Mare (SA), Italy*

[25]*Instituto de Astrofísica e Ciências do Espaço, Universidade de Coimbra, P-T3040-004 Coimbra, Portugal*

[26]*Department of Physics, Sharif University of Technology, PO Box 11155-9161 Tehran, Iran*

[27]*Departamento de Matemática y Física Aplicadas, Facultad de Ingeniería, Universidad Católica de la Santísima Concepción, Alonso de Rivera 2850, Concepción, Chile*

[28]*Centre for Electronic Imaging, Department of Physical Sciences, The Open University, Milton Keynes MK7 6AA, UK*

This paper has been typeset from a TEX/LATEX file prepared by the author.